# Simulation Study of the Aerodynamic Force Distributions on the UAS-S45 Baalam Wing with an Upswept Blended Winglet

Hema AUBEELACK[1,a], Ruxandra Mihaela BOTEZ*,[1,b]

*Corresponding author
*,[1]ÉTS – École de Technologie Supérieure,
Laboratory of Applied Research in Active Controls,
Avionics and AeroServoElasticity,
1100 Notre-Dame St W, Montreal, QC H3C 1K3, Quebec, Canada,
hema.aubeelack.1@ens.etsmtl.ca, ruxandra.botez@etsmtl.ca*

DOI: 10.13111/2066-8201.2019.11.1.2

*Received: 15 January 2019/ Accepted: 09 February 2019/ Published: March 2019*


***Abstract:*** *In this paper, the wing on the Unmanned Aerial System UAS-S45 Bàalam from Hydra Technologies is modeled and studied so that its aerodynamics and baseline performance can be better understood. More specifically, the performance of the wing, with and without a detachable upswept blended winglet, is investigated. Using detailed CFD results, the impact of this winglet is demonstrated through its effect on the spanwise distributions of forces and moments along the wing.*

***Key Words:*** *blended winglet, span-wise distributions, aerodynamic characteristics, UAS-S45 wing*

## I. INTRODUCTION

Winglets are wingtip devices used on fixed-wing aircraft to reduce the drag contribution of wingtip vortices. In this paper, the S45 Bàalam wing designed and manufactured by the Mexican company Hydra Technologies is studied with and without its detachable winglet, so that observations can be made on the influence of the wingtip device on the wing aerodynamics. A review of related published literature on the subject is provided in this section. The modeling technique for the wing without the winglet is described in the Section II, and the representation of the winglet is presented in Section III. In Section IV, the rationale for the test conditions used is provided. The computational approach used is throughly discussed in Section V. Finally, the results obtained are shown and discussed in Section VI.

Three-dimensional flow mechanisms are such that vortices are produced at wing tips as a result of flow leakage. A pressure imbalance between the upper and lower surfaces of the wing is set up because the flow is deflected inwardly on the upper surface, or pressure side, and outwardly on the lower surface, or suction side, leading to the formation of a vortex [1]. This pressure difference, while necessary for the generation of lift, also causes air from the suction side to flow to

[a]M.A.Sc. Student, Research Laboratory in Active Controls, Avionics and Aeroservoelasticity, 1100 Notre-Dame Street West, Montreal, Quebec, Canada.
[b]Full Professor, Research Laboratory in Active Controls, Avionics and Aeroservoelasticity, 1100 Notre-Dame Street West, Montreal, Quebec, Canada, AIAA Associate Fellow.

the pressure side, thereby reducing the effective angle of attack. The lift vector becomes tilted, giving rise to a force component in the opposite direction of the flow called the induced drag [2]. Research on wingtip devices began in the 1970s at NASA with the experimental testing of end plates to reduce the intensity of tip vortices [3, 4] before modern-day winglets. Whitcomb pioneered winglet research by proposing and publishing results for his designs, in which he defined geometric parameters to characterize winglet shape, such as cant, taper, sweep, and toe-out angle [5, 6]. Promptly after Whitcomb's propositions, Heyson et al. used a vortex lattice method to conduct a parametric study on winglet performance, in which they established that, for a given increase in bending moment, a greater reduction in induced drag could be achieved by using a winglet rather than extending the wing tip [7]. They concluded that winglets provide the highest improvement for near-vertical geometries and for high wing loadings near the wing tip.

As the technology readiness level of winglets evolved, numerous patents were filed for novel concepts aimed at wingtip vortex intensity reduction. These patents include blended winglets to eliminate junction discontinuity and vortex concentration at the dihedral corner [8], movably mounted winglets to control the angle of attack and bending moment [9], highly sweptback winglets with low aspect ratio to prevent flow break-away at high lift coefficients [10], spiroid wingtips that loop until they fall back onto the wing [11], elliptical winglets to enforce continuous curvature [12], and multi-winglet variants to attempt to further break down the wingtip vortex [13, 14].

Winglet design garnered attention from sailplane designers such as Maughmer, who used a multiple lifting-line method and a full panel method with relaxed-wake modeling in his works [15, 16]. He concluded that winglet design is a trade-off study because a reduction in induced drag is achieved for a larger wetted area, which is in turn accompanied by an increase in profile drag.

The performance of a winglet is contingent on its design and the flight conditions. As such, optimized designs vary greatly between applications and few generalities exist. Whitcomb suggested that a toe-out angle is needed for good winglet performance, and obtained up to 9% improvement in lift-to-drag ratio and 20% reduction in induced drag at *Re* of $5.25 \times 10^6$, while a wingtip extension provided only 4% improvement on the lift-to-drag ratio for the same change in root bending moment [5]. Smith et al. [14] tested multi-winglets at *Re* from 161,000 to 300,000 and achieved up to 15-30% improvement in lift-to-drag ratio relative to their baseline NACA 0012 wing, observing that dihedral spread helped distribute the vortex. Takenaka et al. [17] performed an optimization in which they minimized the block fuel and maximum takeoff weight to indirectly optimize a winglet in transonic flow using a Euler code. They observed that an abrupt transition encouraged wave drag at the wing-winglet junction, and noted that span length and can't angle held the most influence in their study. A blended winglet was obtained as optimization result, with the winglet leading edge positioned aft of the wing leading edge – corroborating the observation made by Conley [18] on the design of the Learjet that a toe-out angle is important. Marchman et al. [19] established that symmetric winglets are the best suited for general aviation, but have reduced effectiveness on tapered wings.

Eppler [20] showed that positive dihedral yields superior improvements relative to negative dihedral by using a new theory for aerodynamic calculations rather than classical theories with rigid wake models, which yield identical results for both cases.

## II. GEOMETRIC REPRESENTATION

The aerodynamic characteristics of a wing can be studied independently from the rest of an aircraft by considering its equivalent Engineering Sciences Data Unit (ESDU) wing planform [21]. Using this representation, the wing is straightened to remove cranks, if any, and extended into the fuselage by extrapolation. For an already straight-tapered wing planform, such as that of the Hydra

S45 Bàalam (excluding the winglet), this results in a straightforward linear extrapolation to the centre plane of the full aircraft. The resulting equivalent wing is shown in Fig. 1. Mathematically, this linear extrapolation can be expressed as,

$$c_{root,0} = c_{tip} + \frac{b}{b_{wing}}(c_{root} - c_{tip}) \tag{1}$$

The area and span of one equivalent wing are thus, respectively,

$$\begin{aligned} b_{1/2} &= b_{fus} + b_{wing} \\ S_{1/2} &= A_{fus} + A_{wing} \end{aligned} \tag{2}$$

The values of relevant physical parameters for the Hydra S45 Bàalam are summarized in Table 1 and correspond to those indicated in Fig. 1.

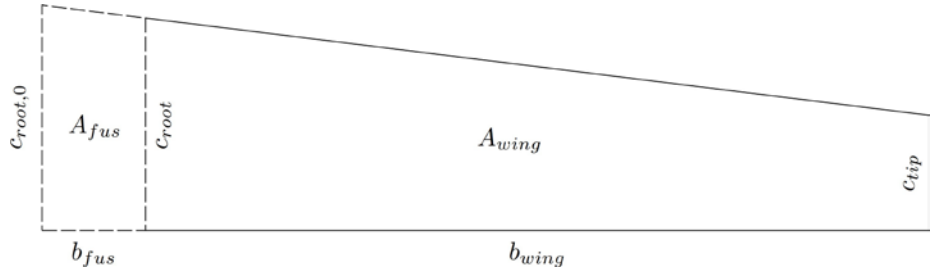


Fig. 1 ESDU representation for a straight-tapered wing

Table 1. Geometric parameters for the Hydra S45 Bàalam

| Symbol | Parameter | Value |
|---|---|---|
| $b_{fus}$ | Fuselage radius (m) | 0.323 |
| $b_{wing}$ | Span of one real wing (m) | 2.450 |
| $b_{1/2}$ | Span of one equivalent wing (m) | 2.773 |
| $c_{root,0}$ | Extrapolated root chord (m) | 0.702 |
| $c_{root}$ | Root chord (m) | 0.665 |
| $c_{tip}$ | Tip chord (m) | 0.359 |
| $A_{fus}$ | Extrapolated fuselage area ($m^2$) | 0.220 |
| $A_{wing}$ | Area of one real wing ($m^2$) | 1.252 |
| $S_{1/2}$ | Area of one equivalent wing ($m^2$) | 1.472 |

The shape of a wing can be further described by additional dimensionless geometric parameters. Two dimensionless characteristics often encountered in aerodynamic wing design are the taper and aspect ratios. A set of angles is used to describe the position of the wing tip relative to the wing root and to account for the three-dimensionality of a wing. Of interest are the sweep and dihedral angles, although others exist. The values for all relevant supplementary parameters are summarized in Table 2.

Table 2. Dimensionless parameters for the Hydra S45 Bàalam

| Symbol | Parameter | Value |
|---|---|---|
| $\lambda$ | Taper ratio | 0.512 |
| $AR$ | Aspect ratio | 10.14 |
| $\Lambda_{c/4}$ | Quarter-chord sweep angle (◦) | 4.8 |
| $\Lambda_{LE}$ | Leading-edge sweep angle (◦) | 6.4 |
| $\Gamma$ | Dihedral angle (◦) | 0 |

A final parameter which describes the wing is the mean aerodynamic chord ($\bar{c}$), which is used as reference length to calculate the chord-based Reynolds number. For a constant taper wing [21], Eq. (3) is obtained, such that $\bar{c}$ is 0.55 m.

$$\frac{\bar{c}}{c_{root,0}} = \frac{2}{3}\frac{1+\lambda+\lambda^2}{1+\lambda} \tag{3}$$

An isometric view of the 3D wing to be analyzed is shown in Fig. 2, with the Cartesian coordinate system displayed. The same definition of coordinate axes is used throughout this work, and the origin is placed at the leading edge of the wing root.

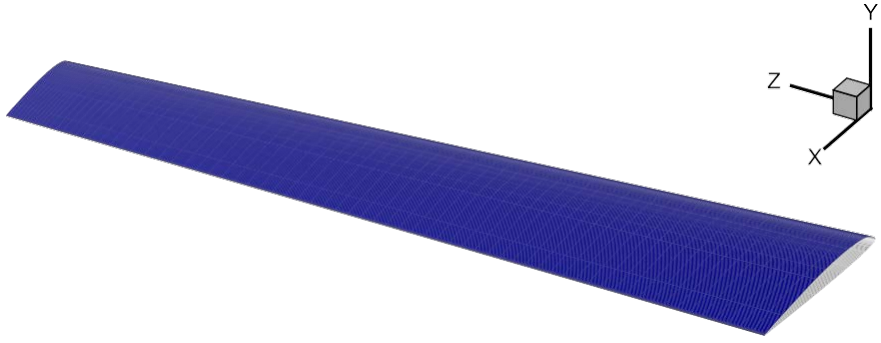


Fig. 2 Isometric view of the 3D wing to be analyzed

## III. REPRESENTATION OF THE UPSWEPT BLENDED WINGLET

The winglet on the Hydra S45 Bàalam is swept upward and backward. The local chord length of the winglet decreases from the interface with the main wing gradually until it vanishes into a point. Owing to the strong curvature which leads to high rates of change in the geometry, the variation of parameters along the span of the winglet was deemed the most efficient way of detailing the winglet geometry. Spanwise distributions are plotted in Fig. 3 for the chord length, and for the leading-edge sweep angle and dihedral angle in Fig. 4. The values are normalized using the span of the winglet ($b_{winglet}$) of 0.206 m. The isometric view for the wing with the winglet attached is presented in Fig. 5.

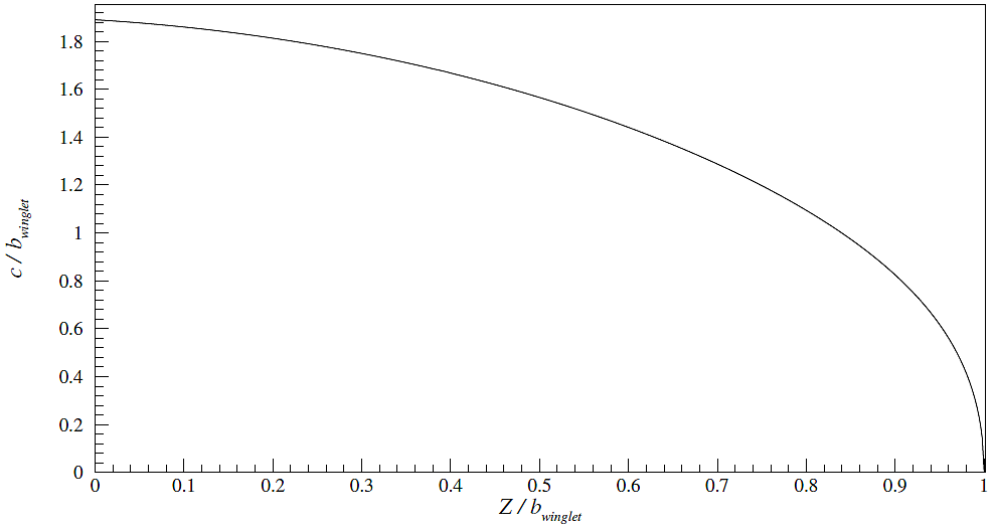


Fig. 3 Spanwise chord length of the Hydra S45 Bàalam winglet

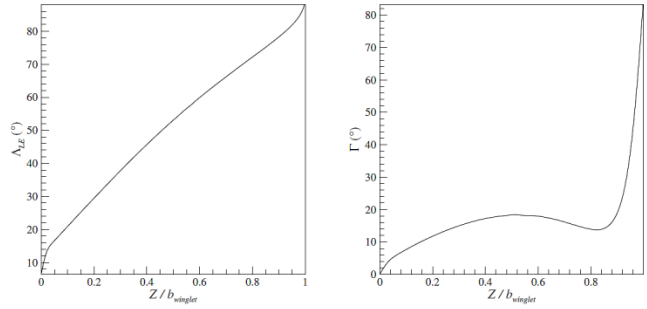


Fig. 4 Spanwise sweep and dihedral angles for the Hydra S45 Bàalam winglet

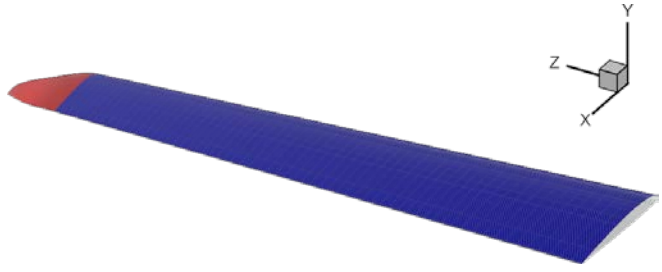


Fig. 5 Isometric view of the wing to be analyzed including the winglet

## IV. FLIGHT CONDITIONS

To determine the aerodynamic performance of the Hydra S45 Bàalam wing, the flow field imposed around the modeled wing needs to be representative of flight conditions typically encountered during missions.

The most important airspeeds in aviation have standard definitions which convey the flight capabilities and normal operation envelope of an aircraft.

The flight characteristics of the UAV deemed useful to gain an understanding of the flow that the wing is subjected to during flight are the stall speed, takeoff speed, cruise speed, never-exceed speed, and velocity of normal operations, whose definitions are given by Jewel [22].

An additional speed, the surveillance speed, is critical here: as a surveillance/reconnaissance UAV, this is the design speed for Hydra S45 Bàalam. All the aforementioned airspeed values for the S45 UAV are summarized in Table 3. Groundspeed, in kt, is the horizontal speed of an aircraft relative to a fixed ground. Indicated airspeed, in knots-indicated airspeed, or kias, is obtained from the dynamic pressure measured by the pitot-static system, and includes wind effects compared to groundspeed.

Table 3. Hydra S45 Bàalam flight characteristics

| Symbol | Parameter | Value |
|---|---|---|
| $V_s$ | Stall speed (kt or kias) | 35 |
| $V_{TO}$ | Takeoff speed (kt) | 40 |
| $V_C$ | Cruise speed (kt) | 50 − 55 |
| $V_{ne}$ | Never-exceed speed (kt or kias) | 90 |
| $V_{no}$ | Velocity of normal operations (kias) | 80 −90 |
| − | Speed of surveillance or patrolling (kias) | 50 −55 |

The typical expected mission profile for a flight for surveillance is illustrated in Fig. 6. The segments lengths are for representation only and do not indicate relative durations of flight segments.The Hydra S45 Bàalam has an autonomy of approximately 12 hours, most of which are

expected to be spent at surveillance or cruise speed. It can be observed that surveillance is carried out at cruise speed.

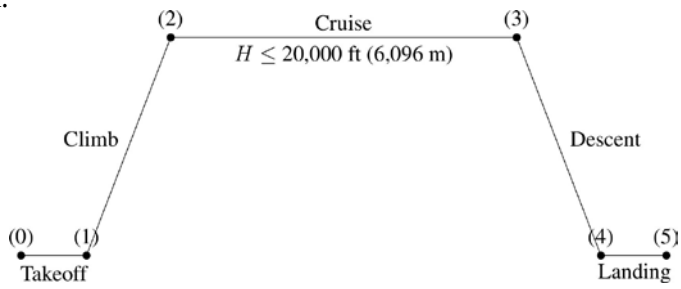


Fig. 6 Typical mission profile for a surveillance UAV

## V. COMPUTATIONAL APPROACH

The flow field around the Hydra S45 Bàalam wing is calculated using CFD software. Pressure and wall shear stress acting on the wing surface are integrated to determine the total force acting on the wing. However, if detailed information on the distribution of forces on different regions on the wing is sought, the full wing surface needs to be partitioned into slices before simulating the flow so that integrations can be performed separately for each slice.

For the wing without the winglet, 20 slices of equal span were used to produce 20 spanwise force and moment values. This number of points was deemed to provide enough points to accurately capture the behaviour of forces and moments along the span of the wing (Fig. 7). For the wing including the winglet, 12 slices of equal span were used for the main wing with an additional 12 logarithmically-spaced slices along the span of the winglet (Fig. 8).

To solve the Navier-Stokes equations using the finite volume method, a grid is constructed to spatially discretize the fluid domain. A multi-block 3D structured grid is generated in ICEM CFD such that element faces are either aligned or normal to the flow direction to minimize the spatial discretization error and error due to numerical diffusion. A high-quality mesh produces more accurate solutions and improves the convergence rate compared to a poorer quality mesh.

Figure 9 shows the grid used to perform the CFD simulations in ANSYS Fluent. The dimensions of the fluid domain are selected far enough from the wing to ensure that the fluid has returned to freestream conditions at the edges of the grid despite the perturbation in the flow field caused by the presence of the wing. Far-field planes are modeled 7 meters ahead and 14 meters behind the origin defined at the leading edge of the wing root. These far-field planes are 14 meters high and 7 meters wide, such that flow at the boundaries can be considered unperturbed by the presence of the wing. The outlet of the fluid domain is placed further than the other boundaries to allow the vortex developing at the wing tip to travel downstream.

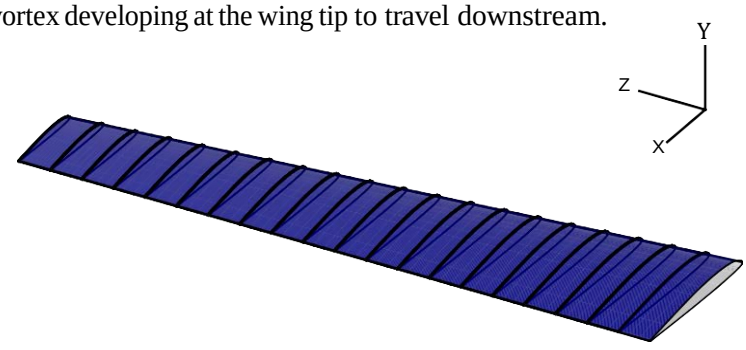


Fig. 7 Sectioned wing without winglet

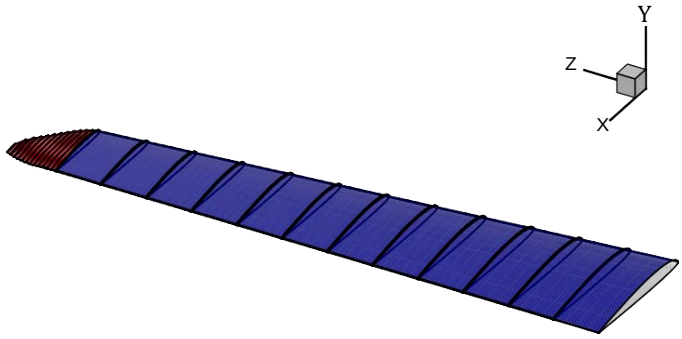


Fig. 8 Sectioned wing with winglet

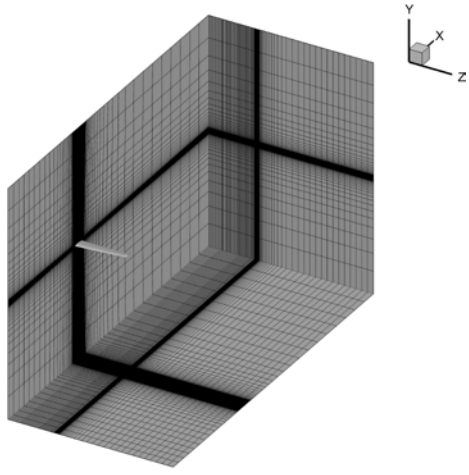


Fig. 9 Finite volume mesh for CFD simulations

An H-grid topology is used in creating the rectangular domain. To finely resolve the boundary layer gradients, an O-grid is used around the wing to create a radially-oriented curvilinear distribution of element edges which become progressively smaller (Fig. 10) as they approach the wing surface. The mesh is also denser at the wing-tip to properly capture the effects of vortices that develop at the wing tip on account of flow leakage.

The rate of change of element sizes is carefully controlled to prevent sudden jumps which can cause a reduction in the order of accuracy of the solution. To prevent backflow and mass imbalance issues at the domain edges behind the wing, which were observed to occur during the development of the meshing procedure, larger cells with higher aspect ratio are used near the domain edges close to the outlet.

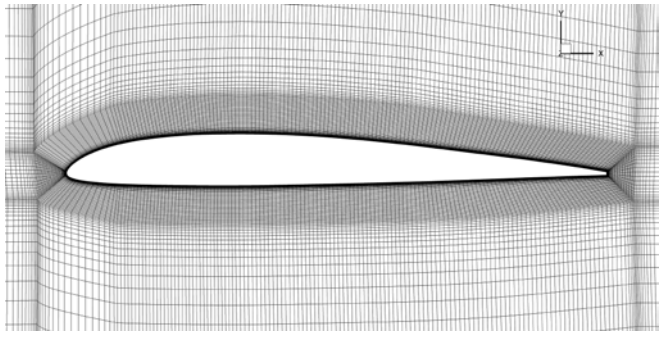

Fig. 10 Boundary layer mesh for CFD simulations

A grid sensitivity study was conducted to determine the mesh density required to produce final results of acceptable fidelity. Five grids of varying resolution were tested at two angles of attack, 0° and 12° at a Reynolds number of $1.0 \times 10^6$, which is the flight condition used in this paper, and close to the upper *Re* limit of $1.07 \times 10^6$ in terms of flight envelope. A $y^+ < 1$ was maintained regardless of the grid under test for the turbulence and transition models to work properly, as mentioned in the previous sub-section. The variations with mesh density of $C_L$, $C_D$, $C_L/C_D$, and laminar-to-turbulent transition location $X/c$ at two spanwise locations $Z/b$ of 0.3 and 0.7 are shown in Tables 4 and 5. In each series of simulations at 0° and 12°, it is observed that the most dense mesh marginally affects the results, which vary asymptotically as the number of cells is increased. The values obtained using the fourth grid are very close to those obtained using the fifth and most dense grid. The differences in the compared values for the two finest grids are below 2% for all the values tested, such that the fourth mesh density is deemed to produce sufficiently accurate results. Based on the grid sensitivity study discussed, the number of cells used for each series of simulations conducted for this paper is shown in Table 6.

Boundary conditions (BCs) are required to solve the difference equations for each fluid volume. Figure 11 shows some of the BCs enforced. A symmetry BC is placed at the right- and left-wing junction, imposing that all property values be the same at -*Z* as those at *Z*, effectively allowing the simulation to be calculated for only one wing. A velocity inlet allows mass flow into the domain at the test velocity, while a pressure outlet allows mass flow out of the domain. Slip walls are imposed on the sides of the far-field to improve convergence, which was observed to be difficult with the transition SST model, particularly with pressure outlets specified for the sides of the far-field. Finally, a no-slip wall BC is enforced at the surface of the wing such that the fluid velocity at the surface is zero. A turbulence intensity of 1%, turbulent viscosity ratio of 10, and an intermittency value of 1 are used at the inlet as turbulence BCs.

Table 4. Grid sensitivity results at $\alpha = 0°$ and $Re = 1.0 \times 10^6$

| **Number of cells** | $C_L$ | $C_D$ | $C_L/C_D$ | $X/c$ at $Z/b = 0.3$ | $X/c$ at $Z/b = 0.9$ |
|---|---|---|---|---|---|
| 1,000,442 | 0.2377 | 0.007605 | 31.26 | 0.4165 | 0.1500 |
| 1,475,928 | 0.2273 | 0.007224 | 31.46 | 0.6395 | 0.5981 |
| 2,274,424 | 0.2218 | 0.006996 | 31.71 | 0.6911 | 0.7015 |
| 3,853,252 | 0.2170 | 0.006792 | 31.94 | 0.7285 | 0.7200 |
| 6,578,640 | 0.2155 | 0.006734 | 32.01 | 0.7313 | 0.7215 |

Table 5. Grid sensitivity results at $\alpha = 12°$ and $Re = 1.0 \times 10^6$

| **Number of cells** | $C_L$ | $C_D$ | $C_L/C_D$ | $X/c$ at $Z/b = 0.3$ | $X/c$ at $Z/b = 0.9$ |
|---|---|---|---|---|---|
| 1,000,442 | 1.403 | 0.07423 | 18.90 | 0.0643 | 0.0615 |
| 1,475,928 | 1.342 | 0.07054 | 19.02 | 0.0805 | 0.0975 |
| 2,274,424 | 1.297 | 0.06759 | 19.19 | 0.1176 | 0.1156 |
| 3,853,252 | 1.266 | 0.06546 | 19.34 | 0.1275 | 0.1367 |
| 6,578,640 | 1.253 | 0.06466 | 19.38 | 0.1280 | 0.1366 |

Table 6. Mesh sizes for CFD simulations

| **Simulation series** | **Number of cells** |
|---|---|
| S45 wing, w/o winglet | 3,873,252 |
| S45 wing, with winglet | 4,883,040 |

A transient formulation was used to overcome convergence difficulties introduced by the transition model and to allow solutions to be obtained at high angles of attack. In this implicit solver, a physical time step size of 0.001 s was found to retain numerical stability, for which 300

total time steps sufficed to obtain a developed solution at the residual target of $1 \times 10^{-5}$ on all flow and turbulence variables.

The combined choice of timestep size and number of time steps is justified by the need for the solution to converge (particularly in the first few timesteps where divergence occurs more readily) which restricts the maximum timestep size, and by the need to achieve a sufficiently developed wing tip vortex to properly account for the induced drag. This is demonstrated in Fig. 12, where a flow visualization image is shown. In this flow visualization, the vortex core can be identified as the thick black line passing in the centre of the shed vortex.

The vortex core extraction method used is the $\lambda_2$ method proposed by Jeong and Hussain [23], where $\lambda_2$, which always takes a negative value, is the second eigenvalue of the symmetric tensor $S^2 + \Omega^2$. The vortex is represented using an iso-surface of $\lambda_2$, where a value of -4275 is used for $\lambda_2$. This value was obtained by examining the contour of $\lambda_2$ in the vortex region shown in Fig. 13 and selecting a value for $\lambda_2$ where the vortex begins roughly.

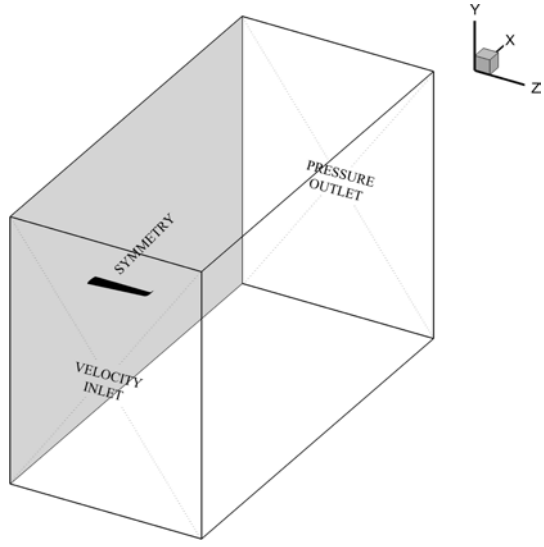


Fig. 11 Boundary conditions for CFD simulations


Fig. 12 Flow visualization of the wing tip vortex at $\alpha = 0°$ and $Re = 1.0 \times 10^6$

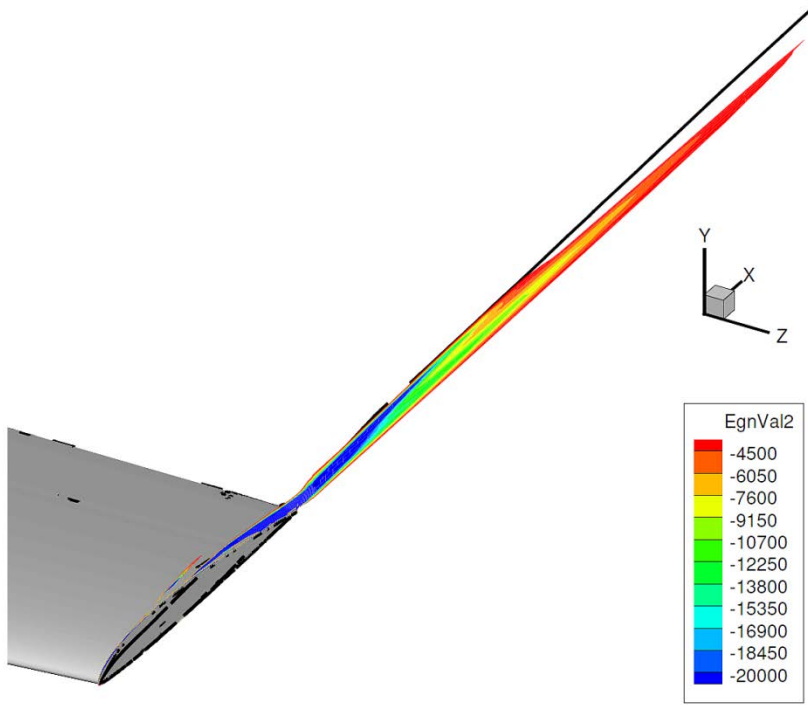


Fig. 13 Contour of $\lambda_2$ near the wing tip at $\alpha = 0°$ and $Re = 1.0 \times 10^6$

The transition SST model is used as turbulence model, with curvature correction, and turbulence kinetic energy production limiter and production Kato-Launder enabled in ANSYS Fluent. A coupled pressure-velocity scheme is used with second-order schemes for the pressure, momentum, $k$, $\omega$, $\gamma$, and $Re_\theta$.

A second-order implicit time discretization is used with the default Courant number of 200, which serves to control the pseudo-time term, as opposed to the physical-time term which is controlled using the time step size [24] (set to 0.001 s). Final values are obtained by time-averaging the results over the last 10 time steps to account for numerical dissipation and small flow fluctuations that may be present.

## VI. RESULTS

The force and moment coefficient variations with the angle of attack obtained from the CFD simulations are plotted in Fig. 14 – 23. Force coefficients are obtained by normalizing the force components using the dynamic pressure and the area of the wing without the winglet. Moment coefficients are obtained by normalizing the moment components using the dynamic pressure, the area of the wing without the winglet, and the mean aerodynamic chord length of the wing without the winglet.

In Fig. 14, the lift coefficient, $C_L$ is plotted against $\alpha$. Loss of lift appears slightly at $\alpha = 12°$ and more evidently at $\alpha = 14°$ as a larger portion of the wing begins to stall. $C_L$ for the wing equipped with the winglet is consistently superior to that for the plain wing. The supplementary $C_L$ takes the shape of an inverted parabola, taking a value of 0.0092 at $\alpha = 0°$ and increasing decreasingly to 0.037 at $\alpha = 14°$. The percentage increase in $C_L$ relative to the plain wing owing to the winglet is largest at $\alpha = 0°$ with 4.23%, and sporadically decreases to 2.31% at $\alpha = 10°$, point at which it increases again.

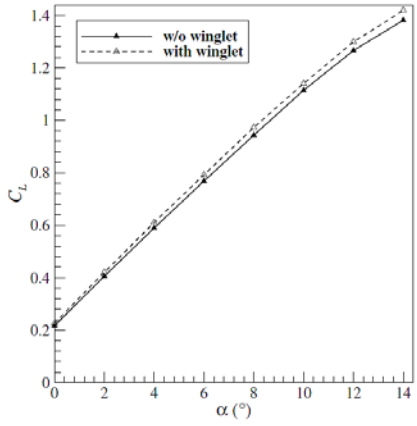


Fig. 14 Lift curve for the S45 wing

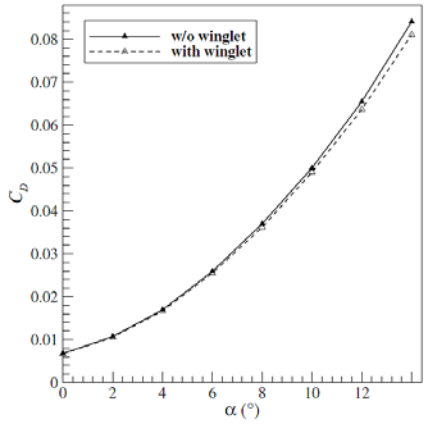


Fig. 15 Drag curve for the S45 wing

In Fig. 15, the drag coefficient, $C_D$ is plotted. This total drag coefficient is the sum of two components, one due to the pressure field, $C_{D,pres}$ and the other due to wall shear stress, $C_{D,visc}$. The $C_D$, pres and $C_{D,visc}$ curves are shown in Fig. 16 and Fig. 17, respectively. From this drag breakdown, the belief that all components of drag except for frictional drag vary as $C_L^2$ is confirmed. This relationship implies that a plot of $C_D$ against $C_L^2$ is a straight line, so long as no part of the wing begins stalling. On the horizontal axis, $C_L^2 = 0$, which, when used in the best linear fit equation, yields the zero-lift drag coefficient, $C_{D,0}$. Using values for $\alpha$ = 0° to 10°, the linear approximation $C_D = 10^{-3}\cdot(36.3C_L^2 + 4.72)$ with a coefficient of determination $R^2 = 0.99973$ is obtained for the wing without the winglet. Similarly, $C_D = 10^{-3}\cdot(34.7C_L^2 + 4.51)$ with $R^2 = 0.99936$ is obtained for the wing equipped with the winglet. As a result, $C_{D,0}$ values are obtained as $4.72 \times 10^{-3}$ and $4.51 \times 10^{-3}$ for the wing without and with the winglet, respectively. This difference represents a 4.45% reduction in $C_{D,0}$ of the plain wing, and is likely due to the distribution of increasingly short chord lengths along the winglet. Shorter local chords are responsible for lower local Reynolds numbers, placing a greater proportion of the wing in a laminar flow regime and thus lowering $C_{D,0}$ overall.

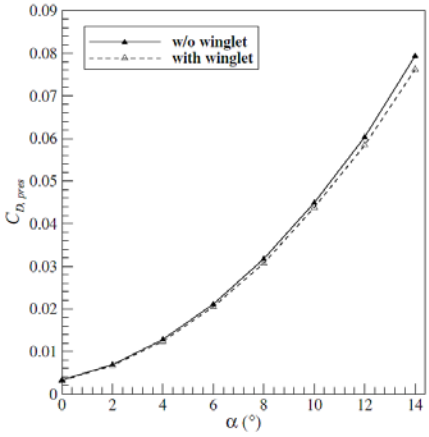


Fig. 16 Pressure drag curve for the S45 wing

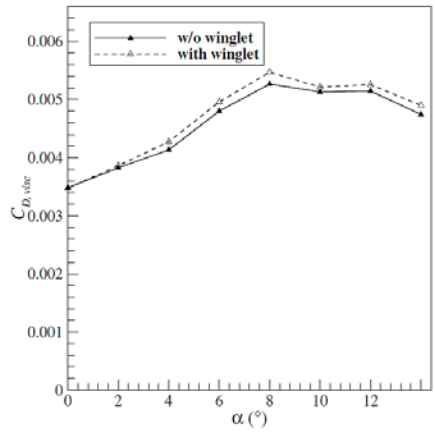


Fig. 17 Viscous drag curve for the S45 wing

Values for $C_D$ are observed to be consistently lower when the winglet is used (Fig. 15). Figure 17 demonstrates that the viscous drag, $C_{D,visc}$, behaves in approximately the same way for the wing without or with the winglet. This entails that the differences in $C_D$ are, by and large, sensibly exclusively attributable to $C_{D,pres}$ differences. This implication is in keeping

with the known behaviour of winglets in that their primary objective is to reduce the intensity of wing-tip vortices and therefore the induced drag. Comparing $C_{D,pres}$ values, the reduction obtained increases increasingly with the angle of attack, from $0.09 \times 10^{-3}$ at $\alpha = 0°$ to $3.17 \times 10^{-3}$ at $\alpha = 14°$. The percent improvements on $C_{D,pres}$ do not vary much with α and exhibit no particular trend, with values between 2.42 and 3.98% and an average of 3.06%, relative to the plain wing. Lastly, comparing $C_D$ values, the reduction obtained increases increasingly with the angle of attack (as was observed with $C_{D,pres}$) from $0.09 \times 10^{-3}$ at $\alpha = 0°$ to $3.013 \times 10^{-3}$ at $\alpha = 14°$. The corresponding percent improvements on $C_D$ show a slow increase between $\alpha = 0°$ and 10°, from 1.39% to 2.00%, followed by a more pronounced increase between $\alpha = 10°$ and 14°, from 2.00% to 3.58%. This shift in slope can be explained by considering the relative influence of each drag component on the total drag: at lower $\alpha$, $C_{D,visc}$ is of greater proportion of the total drag, but, as α increases, $C_{D,pres}$ increases much more quickly and growingly dominates in the total drag. From $\alpha = 0°$ to 14°, $C_{D,pres}$ goes from constituting 51.3% of the total drag down to only 5.64% on the plain wing, and from 51.9% to 6.04% on the wing with the winglet.

The glide ratio represents the ratio of lift force to drag force. Its variation is shown in Fig. 18. It is a direct consequence of the previously discussed results. An increase in $C_L$ accompanied by a decrease in $C_D$ leads to a percent increase in $C_L/C_D$ of the combined individual percent improvements on $C_L$ and $C_D$. $(C_L/C_D)_{max}$ occurs in the neighborhood of $\alpha = 2°$ (as is confirmed by drawing a tangent to the curve going through the origin), where $C_L/C_D$ values are 37.77 and 39.82 for the wing without and with the winglet, respectively. This difference represents a 5.42% increase in $(C_L/C_D)_{max}$. The $C_L$-$C_D$ plot, better known as the drag polar, is shown in Fig. 19. This final plot also reflects the previously discussed observations on the enhanced aerodynamic performance of the wing with the winglet.

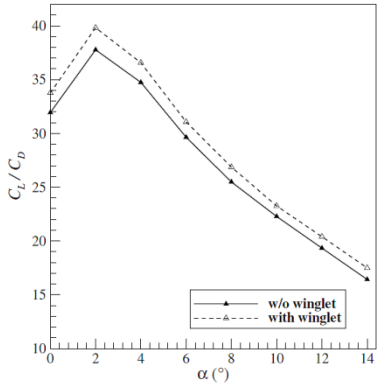


Fig. 18 Lift-to-drag curve for the S45 wing

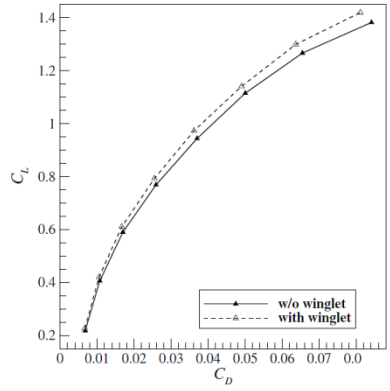


Fig. 19 Drag polar for the S45 wing

Figure 20 shows the variation of the side force coefficient ($C_Y$) with α. $C_Y$ during steady level flight for a wing has very little effect on the motion of the aircraft in the absence of crosswinds, mainly because the right and left wing produce equal and opposite side forces in such a symmetrical flow. The presence of the winglet causes a decreasing decrease in $C_Y$ with $\alpha$, with a decrement of $1.85 \times 10^{-3}$ at $\alpha = 0°$ to $6.55 \times 10^{-3}$ at $\alpha = 14°$. This corresponds to a 66.5% decrease in $C_Y$ relative to the plain wing at $\alpha = 0°$ which gradually reduces to a 15.0% decrease at $\alpha = 14°$.

Figure 21 shows the yaw moment coefficient ($C_n$) curve with $\alpha$. Similarly, Fig. 22 shows the roll moment coefficient ($C_l$) curve and Fig. 23 show the pitching moment coefficient ($C_m$) curve with $\alpha$. The moments are calculated based on the forces on the wing presented previously acting at the center of pressure. From the coordinate system established, the forces along the *x*-, *y*-, and *z*-axes are non-

dimensionally $C_D$, $C_L$ and $C_Y$, respectively, while the moments are $C_l$, $C_n$, and $C_m$, respectively. As such, when a force is parallel to the moment axis, it produces no moment. $C_l$, $C_n$, and $C_m$ are all greater in magnitude for the wing equipped with the winglet relative to the plain wing. For both the right and left wings in a symmetrical flow, $C_l$ and $C_n$ have a zero resultant. $C_m$ for both wings, however, is twice the value plotted in Fig. 23. The difference in $C_m$ values introduced by the winglet is nearly linear, such that $C_m$ is, on average, 5.60% higher for the wing equipped with the winglet relative to the plain wing. Beyond the relatively global analysis of the impact of the winglet in terms of force and moment coefficients that has been done thus far in this series of results, more can be understood about how the behaviour of the flow changes in the presence of the wingtip device. Specifically, the force along the span of the wing can be plotted to paint a clearer picture of winglet aerodynamics. A force-per-unit-span measure is used, such that the spanwise integral thereof representing the area under the curve yields the total force. In Fig. 24, the lift force per unit span, $L'$, is plotted for $\alpha = 0°$ to 14° every 2°. Likewise, the drag force per unit span, $D'$, is plotted in Fig. 25, and shown again in more detail in the wingtip region in Fig. 26. The side force per unit span, $Y'$, is shown in Fig. 27.

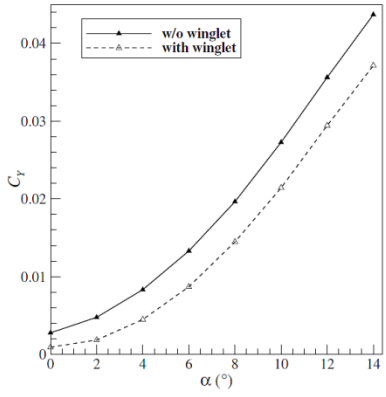


Fig. 20 Side force curve for the S45 wing

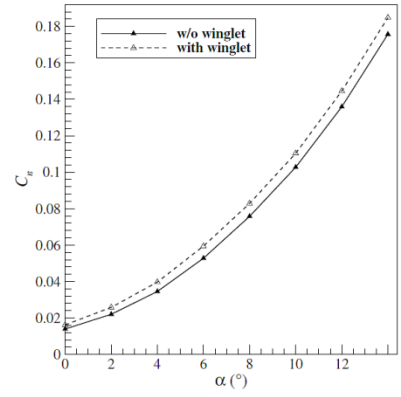


Fig. 21 Yaw moment curve for the S45 wing

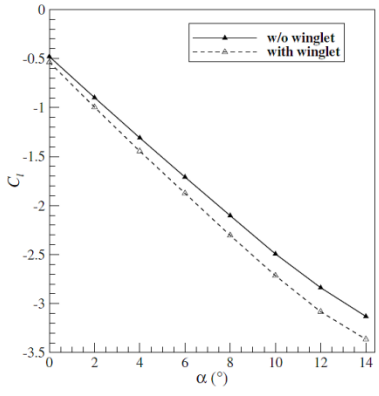


Fig. 22 Roll moment curve for the S45 wing.

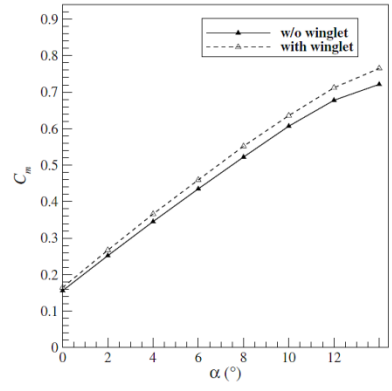


Fig. 23 Pitching moment curve for the S45 wing

A prominent feature present in the spanwise force distributions is the jump in properties at the wing-winglet junction, which is likely attributable to the discontinuity in the rate of change of sweep and dihedral angles, and to a greater degree to the sudden rate of change in chord length and therefore area. The $L'$ distribution demonstrates little beyond an extension in the span and a discontinuity in the wing area. The $D'$ distribution shows lower drag on the wing with the winglet, which is representative of the reduction in induced drag. The more detailed $D'$ distribution also indicates that at low angles of attack (at $\alpha$ = 0° and 2° in Fig. 26), the drag for a small

portion of the span is negative owing to the surface curvature of the winglet. Considering the *Y'* distribution, diminished side force values are observed on the winglet relative to the wingtip of the plain wing. The *D'* and *Y'* distributions indicate that, in all likelihood, part of the force that would conventionally be the side force acts in the reverse direction of drag when the winglet is affixed to the wingtip of the plain wing. The *Y'* distribution also shows the development of a negative component induced by the winglet; this supplements the previous observation that $C_Y$ is consistently lower with the winglet by making evident the negative portions that serve to reduce the total side force value.

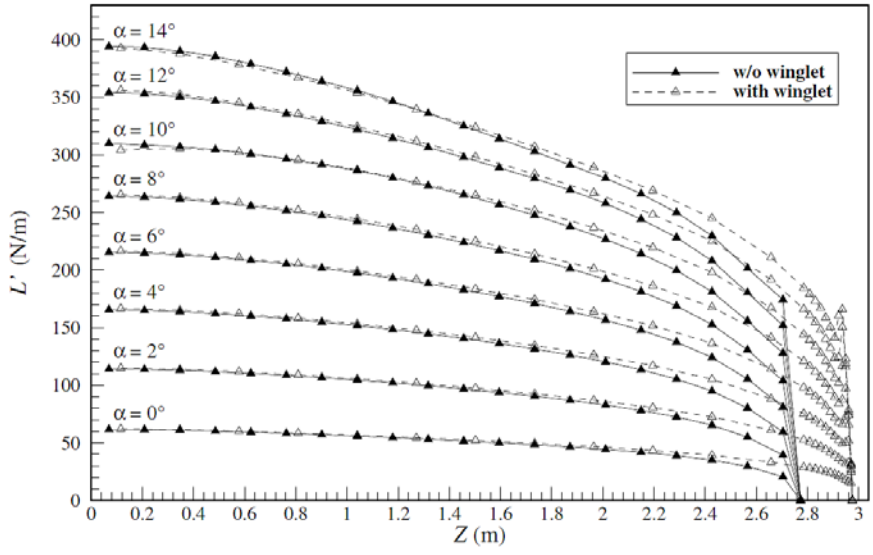


Fig. 24 Spanwise lift distribution for the S45 wing

Finally, images of the wing tip vortices are shown in Fig. 28 – 35 to illustrate the impact of adding the winglet studied in this chapter and to confirm that these vortices have been properly resolved. The wing tip vortices appear to be consistently weaker for the wing equipped with the winglet relative to the wing without the winglet.

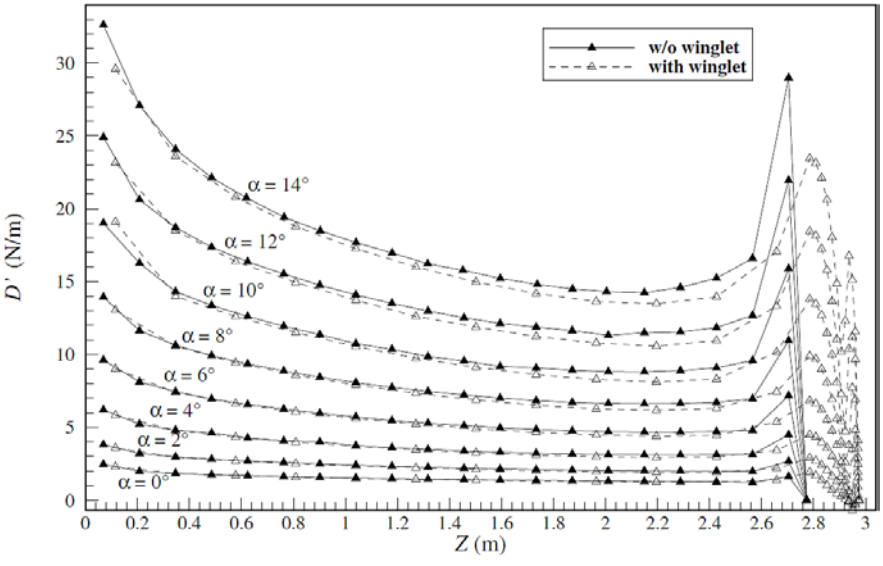


Fig. 25 Spanwise drag distribution for the S45 wing

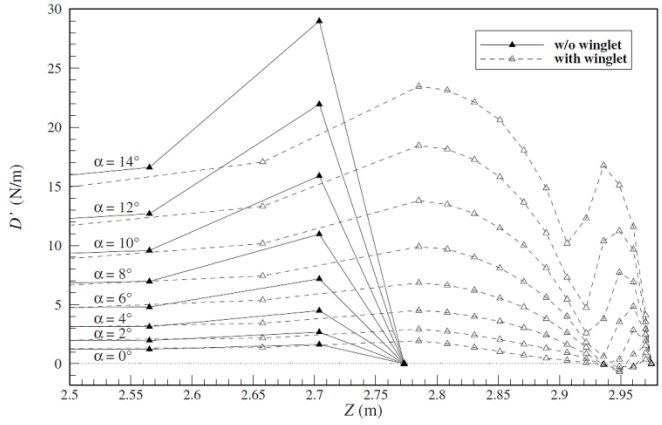


Fig. 26 Close-up view of the spanwise drag distribution near the wing tip

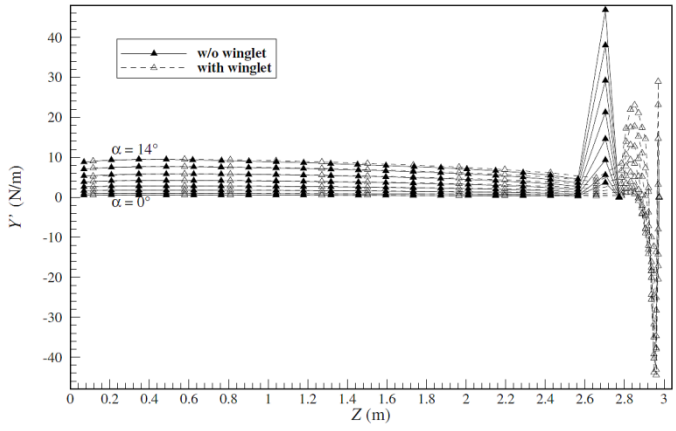


Fig. 27 Spanwise side force distribution for the S45 wing

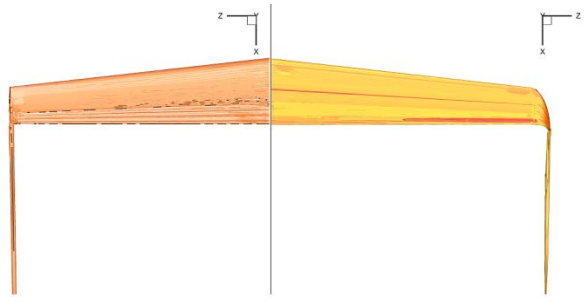

Fig. 28 Wing tip vortex visualizations without and with the winglet at α = 0° and *Re* = 1.0 × $10^6$

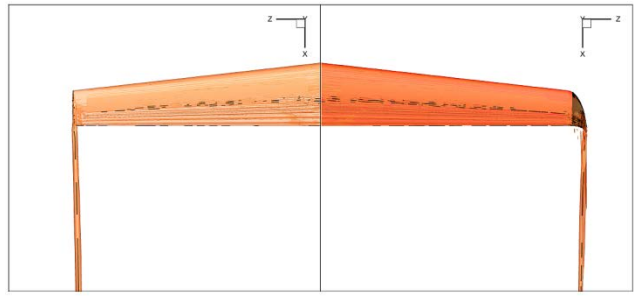

Fig. 29 Wing tip vortex visualizations without and with the winglet at α = 2° and *Re* = 1.0 × $10^6$

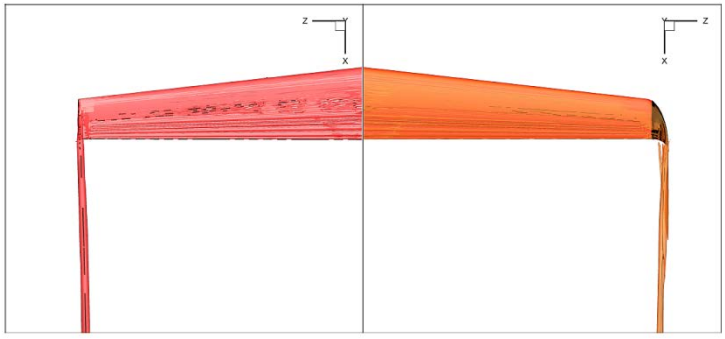

Fig. 30 Wing tip vortex visualizations without and with the winglet at $\alpha = 4°$ and $Re = 1.0 \times 10^6$

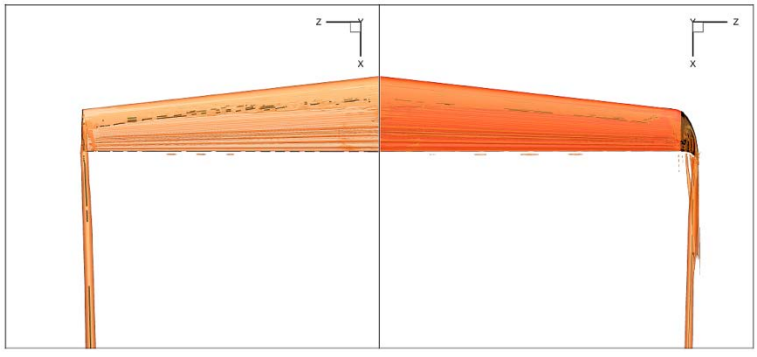

Fig. 31 Wing tip vortex visualizations without and with the winglet at $\alpha = 6°$ and $Re = 1.0 \times 10^6$

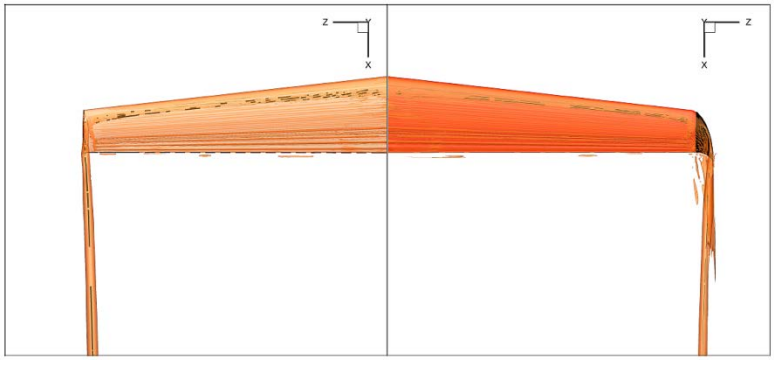

Fig. 32 Wing tip vortex visualizations without and with the winglet at $\alpha = 8°$ and $Re = 1.0 \times 10^6$

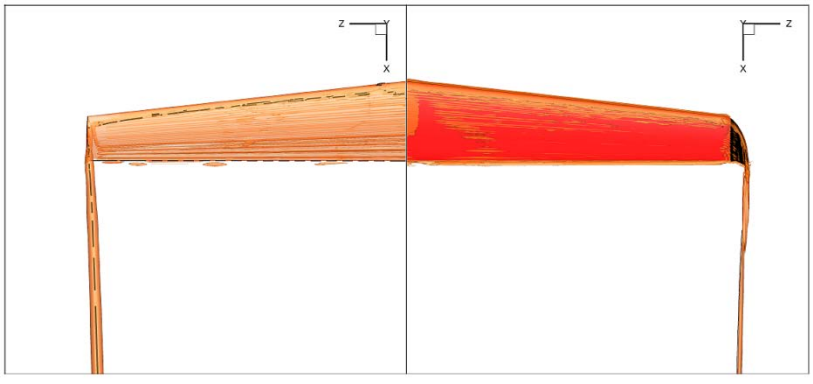

Fig. 33 Wing tip vortex visualizations without and with the winglet at $\alpha = 10°$ and $Re = 1.0 \times 10^6$

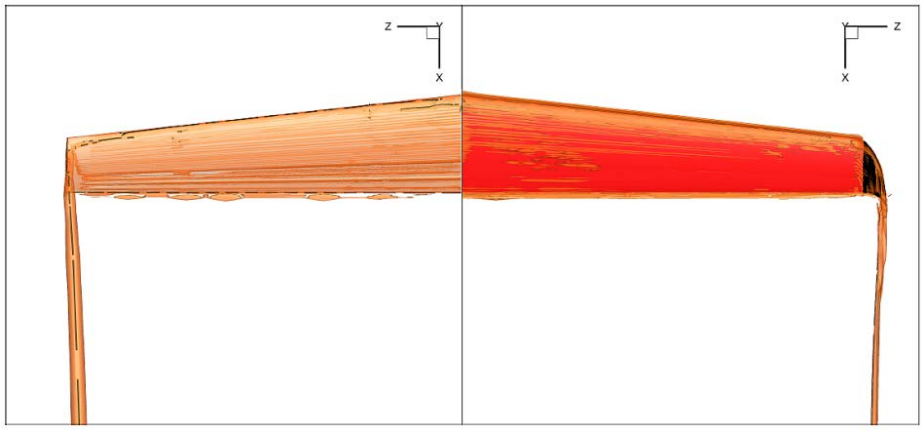


Fig. 34 Wing tip vortex visualizations without and with the winglet at $\alpha = 12°$ and $Re = 1.0 \times 10^6$

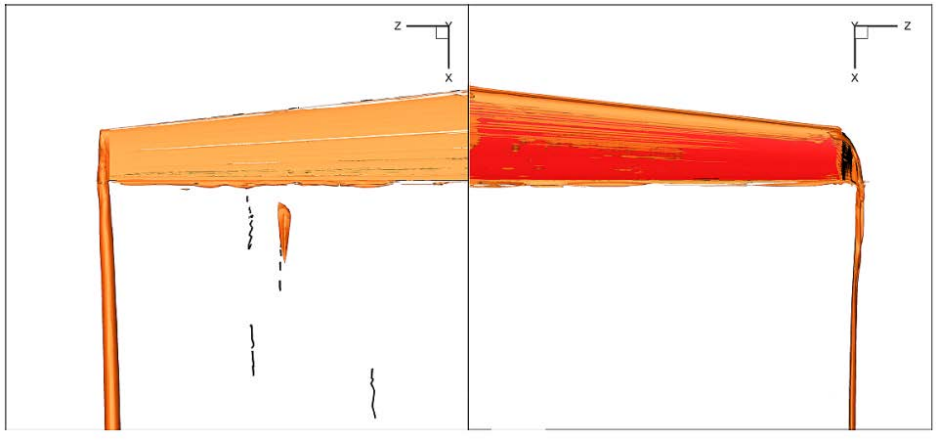


Fig. 35 Wing tip vortex visualizations without and with the winglet at $\alpha = 14°$ and $Re = 1.0 \times 10^6$

## VII. CONCLUSIONS

In this paper, CFD results are explored in detail and presented for the S45 Baalam from Hydra Technologies. Other aerodynamic research was done on the UAS-S4, that was designed and manufactured by Hydra Technologies prior to the UAS-S45, as seen in [25]- [28].

From the series of CFD simulations conducted, it is clear that the upswept blended winglet on the S45 Bàalam brings a noteworthy improvement in aerodynamic performance. The moment coefficients for the wing change significantly with the introduction of the winglet, suggesting that there could be more underlying mechanisms to be understood about this winglet in relation to aircraft stability.

## ACKNOWLEDGEMENTS

Special thanks are dues to the Natural Sciences and Engineering Research Council of Canada (NSERC) for the Canada Research Chair Tier 1 in Aircraft Modelling and Simulation Technologies funding. We would also like to thank Mrs. Odette Lacasse and Mr. Oscar Carranza for their support at the ETS, as well as to Hydra Technologies' team members Mr. Carlos Ruiz, Mr. Eduardo Yakin and Mr. Alvaro Gutierrez Prado in Mexico.

## REFERENCES


[1] D. McLean, *Understanding aerodynamics: arguing from the real physics*, John Wiley & Sons, 2012.
[2] J. D. Anderson Jr., *Fundamentals of aerodynamics*, Tata McGraw-Hill Education, 2010.
[3] P. E. Hemke, Drag of wings with end plates, *NACA Rep. 267*, 1928.
[4] W. Mangler, The lift distribution of wings with end plates, *NACA TM-856*, 1938.
[5] R. T. Whitcomb, A design approach and selected wind tunnel results at high subsonic speeds for wing-tip mounted winglets, *NASA TN D-8260*, 1976.
[6] R. T. Whitcomb, Methods for reducing aerodynamic drag, *NASA Conference Publication*, Vol. **2211**, pp. 10–13, 1981.
[7] H. H. Heyson, G. D. Riebe and C. L. Fulton, Theoretical parametric study of the relative advantages of winglets and wing-tip extensions, *NASA TP 1020*, 1977.
[8] R. V. Finch, *Vortex reducing wing tip*, US Patent 4,108,403, 1978.
[9] M. Daude, *Winglets for aircraft wing tips*, US Patent 4,457,479, 1984.
[10] J. A. Jupp and P. H. Rees, Aircraft wing and winglet arrangement, US Patent 4,714,215, 1987.
[11] L. B. Gratzer, *Spiroid-tipped wing*, US Patent 5,102,068, 1992.
[12] F. F. Felker, *Aircraft with elliptical winglets*, US Patent 6,484,968, 2002.
[13] U. La Roche and S. Palffy, Wing-grid, a novel device for reduction of induced drag on wings, *ICAS Proceedings*, Vol. **20**, pp. 2303–2309, 1996.
[14] M. Smith, N. Komerath, R. Ames, O. Wong and J. Pearson, Performance analysis of a wing with multiple winglets, *19th AIAA Applied Aerodynamics Conference, Anaheim, CA, USA*, doi:10.2514/6.2001-2407, 2001.
[15] M. D. Maughmer, Design of winglets for high-performance sailplanes, *Journal of Aircraft*, Vol. **40**, No. 6, pp. 1099–1106, 2003.
[16] M. D. Maughmer, The design of winglets for low-speed aircraft, *Technical Soaring*, Vol. **30**, No. 3, p. 6173, 2006.
[17] K. Takenaka, K. Hatanaka, W. Yamazaki and K. Nakahashi, Multidisciplinary design exploration for a winglet, *Journal of Aircraft*, Vol. **45**, No. 5, p. 1601, 2008.
[18] N. Conley, Winglet toe-out angle optimization for the gates Learjet longhorn wing, *Journal of Aircraft*, Vol. **17**, No. 12, pp. 851–855, 1980.
[19] I. Marchman, D. Manor and H. Faery Jr., Whitcomb winglet applications to general aviation aircraft, *Aircraft Systems and Technology Conference*, p. 1478, 1978.
[20] R. Eppler, Induced drag and winglets, *Aerospace science and Technology*, Vol. **1**, No. 1, pp. 3–15, 1997.
[21] * * * ESDU, I., *Geometrical properties of cranked and straight-tapered wing planforms*, 1976.
[22] J. W. Jewel, Operational Experiences of General Aviation Aircraft, *Conference on Aircraft Operating Problems, NASA SP-83*, 1965.
[23] J. Jeong and F. Hussain, On the identification of a vortex, *Journal of fluid mechanics*, Vol. **285**, pp. 69–94, 1995.
[24] * * * ANSYS Inc., F., Introductory FLUENT Training: Solver Settings, FLUENT v6.3, 2006.
[25] O. Sugar Gabor, A. Simon, A. Koreanschi, R. M. Botez, Aerodynamic Performance Improvement of the UAS-S4 Éhecatl Morphing Airfoil Using Novel Optimization Techniques, *Proceedings of the Institution of Mechanical Engineers, Part G: Journal of Aerospace Engineering*, Vol. **230**, No. 7, 2015.
[26] O. Sugar Gabor, A. Simon, A. Koreanschi, R. M. Botez, Improving the UAS-S4 Éhecatl Airfoil High Angles-of-Attack Performance Characteristics using a Morphing Wing Approach, *Proceedings of the Institution of Mechanical Engineers, Part G: Journal of Aerospace Engineering*, Vol. **230**, No. 1, pp. 118-131, 2016.
[27] O. Sugar Gabor, A. Koreanschi, R. M. Botez, Analysis of UAS-S4 Éhecatl Aerodynamic Performance Improvement using Several Configurations of a Morphing Wing Technology, *The Aeronautical Journal*, Vol. **120**, No. 1231, pp. 1337-1364, 2016.
[28] O. Sugar Gabor, A. Koreanschi, R. M. Botez, A New Non-Linear Vortex Lattice Method: Applications to Wing Aerodynamic Optimizations, *Chinese Journal of Aeronautics*, Vol. **29**, No. 5, pp. 1178-1195, 2016.